THE JOURNAL OF PHYSICAL CHEMISTRY C
A JOURNAL OF THE AMERICAN CHEMICAL SOCIETY

pubs.acs.org/JPCC

Article

Hydrogenated Carbon Monolayer in Biphenylene Network Offers a Potential Paradigm for Nanoelectronic Devices

Salih Demirci, Taylan Gorkan, Şafak Çallıoğlu, V. Ongun Özçelik, Johannes V. Barth, Ethem Aktürk,* and Salim Ciraci*

Cite This: *J. Phys. Chem. C* 2022, 126, 15491−15500

Read Online

ABSTRACT: A metallic carbon monolayer in the biphenylene network (specified as C ohs) becomes an insulator upon hydrogenation (specified as CH ohs). Patterned dehydrogenation of this CH ohs can offer a variety of intriguing functionalities. Composite structures constituted by alternating stripes of C and CH ohs with different repeat periodicity and chirality display topological properties and can form heterostructures with a tunable band-lineup or Schottky barrier height. Alternating arrangements of these stripes of finite size enable one to also construct double barrier resonant tunneling structures and 2D, lateral nanocapacitors with high gravimetric capacitance for an efficient energy storage device. By controlled removal of H atom from a specific site or dehydrogenation of an extended zone, one can achieve antidoping or construct 0D quantum structures like antidots, antirings/loops, and supercrystals, the energy level spacing of which can be controlled with their geometry and size for optoelectronic applications. Conversely, all these device functions can be acquired also by controlled hydrogenation of a bare C ohs monolayer. Since all these processes are applied to a monolayer, the commensurability of electronically different materials is assured. These features pertain not only to CH ohs but also to fully hydrogenated Si ohs.

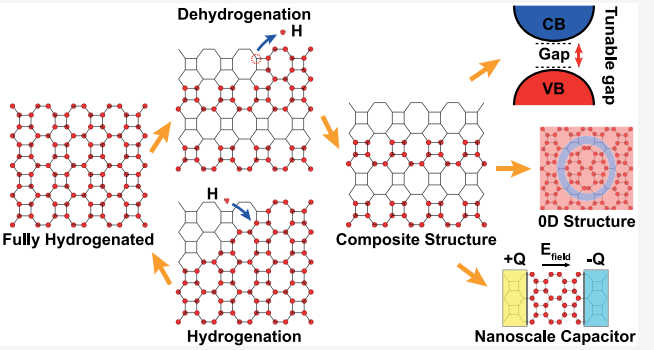

INTRODUCTION

A two dimensional monolayer of carbon in a biphenylene network has been proposed/predicted by various theoretical studies[1−6] as an alternative to the well-known graphene. Recently, the synthesis of this 2D nonhexagonal, monolayer structure (which consists of the adjacent octagon- (*o*), hexagon- (*h*), and square- (*s*) rings and is specified briefly as *C ohs structure* in this text) have been realized using different processes.[7,8] Even if the 3-fold coordination of atoms is maintained in this new allotrope, the sp^2-hybridization is deformed. Very recently, we showed[9] that not only the C ohs structure, but also stable ohs monolayers of other group IV elements (Si, Ge), group IV−IV (SiC, GeC, SnC), III−V (BN, BP, BAs, BSb, AlN, AlP, GaN, InN), and II−VI (ZnSe) compounds and their multilayers, as well as 3D periodic ohs crystals, can be regarded a new class of materials like their counterparts in the honeycomb network.[10−14] Here, C, Si, and Ge ohs monolayers of group IV elements have been found to be good metals as a consequence of multiple crossing of the Fermi level by p_z-bands, in contrast to their Dirac semimetal counterparts in a honeycomb network, namely graphene,[15] silicene, and germanene.[10−14] Recent studies on the adsorption of adatoms like H, O, C, Si, F, Ti, and Gd on bare C ohs monolayer have predicted various critical effects on the electronic properties.[16−20] In particular, it has been demonstrated that C and Si ohs monolayers can acquire novel magnetic and electronic states. These functional properties are tunable by the coverage of diverse adatoms, by the formation of vacancy and other point defects.[20] Other properties related with C ohs have been reported in recent papers.[21,22]

In this study, we show that on a 2D monolayer one can realize a number of crucial electromagnetic device functions. This can be achieved either by modulating dehydrogenation on the same insulating CH ohs (i.e., fully hydrogenated C ohs) or by hydrogenation on the metallic C ohs. Furthermore, not only C ohs/CH ohs but also Si/SiH ohs monolayers exhibit similar behavior via controlled dehydrogenation or hydrogenation. Patterned dehydrogenation (hydrogenation) of CH (C) ohs monolayers can be explored as a novel process in nanoelectronics.

Received: June 27, 2022
Revised: August 17, 2022
Published: August 30, 2022

https://doi.org/10.1021/acs.jpcc.2c04453
J. Phys. Chem. C 2022, 126, 15491−15500

METHODS

Calculations based on the density functional theory (DFT) were carried out using VASP[23] packages. Projector-augmented wave potentials[24] and the exchange-correlation potential within the generalized gradient approximation with the Perdew, Burke, and Ernzerhof (PBE) functional[25] have been used. Electronic wave functions have been expanded by plane-wave basis sets up to the electron kinetic energy cutoff of 520 eV. The dipole correction and the van der Waals correction within the method of Grimme (DFT-D3)[26,27] have been taken into account. Brillouin zone (BZ) integration was performed with a Γ-centered k-point grid in the Monkhorst−Pack scheme.[28] A dense k-mesh like 12 × 7 × 1 has been used for the primitive cells based on a convergence analysis; the k-mesh has been rescaled according to the size and symmetry of the supercells used in each calculation. Ionic relaxation was realized by a conjugate gradient algorithm. All atoms in the supercell have been relaxed until the energy difference between the successive steps was less than 10^{-5} eV and the force on each atom was less than 10^{-2} eV/Å. In addition, maximum pressure on the lattice has been lowered down to 0.1 kbar. Also, the Heyd−Scuseria−Ernzerhorf (HSE06) hybrid functional method[29] is applied to obtain corrected band gap values. The HSE06 functional is constructed by mixing 25% of the Fock exchange with 75% of the PBE exchange and 100% of the PBE correlation. Surface state calculations are performed using the WannierTools package[30] based on the tight binding Hamiltonians constructed from maximally localized Wannier functions (MLWFs) as implemented in the Wannier90 code[31] in conjunction with the VASP packages. All calculations of finite size capacitors under lateral electric field have been performed using local basis set.[32]

The dynamical stability analysis, which is crucial for monolayers coated with adatoms, was performed by using the density functional perturbation theory (DFPT), to calculate phonon spectra.[33] The structures having vibration modes with frequencies $\omega^2 > 0$ for all k in the first BZ are considered to be stable. The thermal stability of these systems is tested by *ab initio* molecular dynamics calculations at finite temperature (AIMD). The time step between ionic iterations was taken to be 2 fs. After every 50 steps, velocities are rescaled to match the desired temperature. The net charge on selected adatoms is calculated by Bader analysis.[34] All the structures were visualized in the VESTA code.[35]

RESULTS

Hydrogen Coverage. Although each atom of the bare C ohs monolayer is an active site to bind H adatom, the saturation of nearest C atoms by H atom is unfavorable energetically. Hence a full hydrogenation of C ohs through the saturation of all C atoms from only one side cannot occur. However, half-coverage by saturating C atoms by H adatoms alternatingly from a single side (specified as C_2H ohs) can be realized, whereby the unit cell is doubled. While the C ohs monolayer is a stable, strictly 2D metal with planar geometry, the free-standing C_2H ohs with the atomic structure depicted in Figure 1a, gains an energy of 6.10 eV per cell and has dynamical and thermal stability unless $\mathbf{k} \rightarrow 0$. Its stability is assured by extensive stability analysis (see Methods). As a result, carbon atoms bound to H are buckled, whereby the deformed sp^2-hybridization changes to sp^3-like bonding and the system turns to be a semiconductor. As shown in parts a and b of Figure 1, C_2H ohs is a long-ranged ferromagnetic semiconductor with a magnetic moment of μ_T = 2.0 μ_B/cell, where the indirect band gap $E_{g,i}$, of spin up and spin down states is 1.72 and 1.67 eV, respectively. Not only the electronic structure, but also the mechanical properties differ from those of the parent C ohs monolayer; the Poisson's ratio, ν_x and ν_y, decreased more than 50% as seen in Table 1. Apparently, the

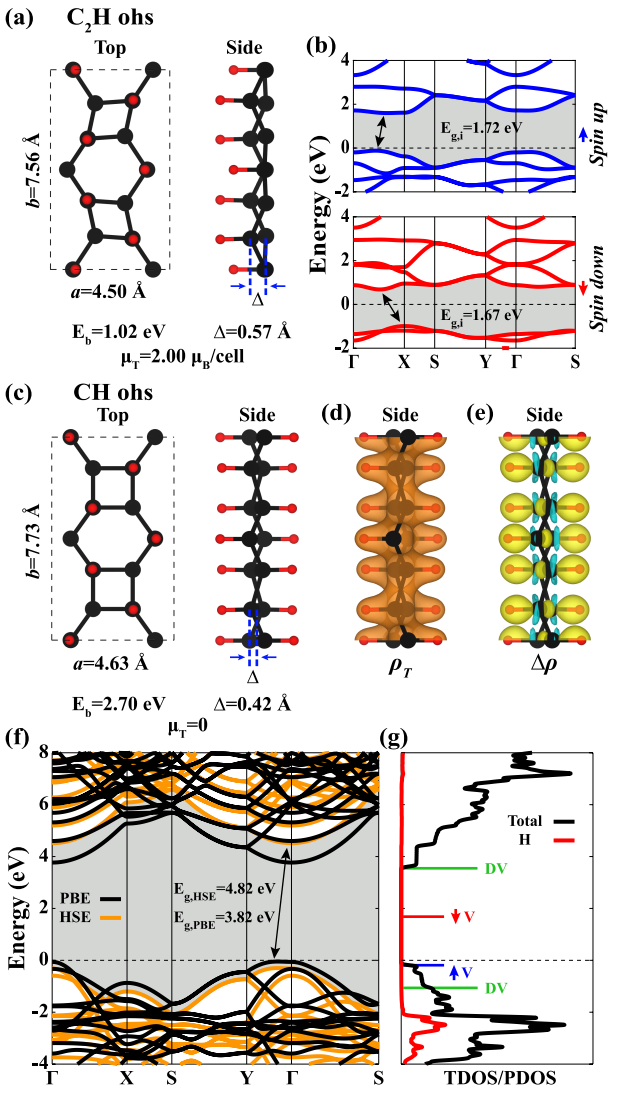

Figure 1. (a) Top and side views of the atomic structure of half, hydrogen covered C ohs, namely C_2H ohs with large-black and small-red balls indicating C and H ohs atoms, respectively. The cell is delineated and lattice constants, a and b, and buckling Δare indicated. (b) Energy band structures for spin up and spin down states with their band gaps shaded. (c) CH ohs (i.e., C ohs full hydrogen covered from both sides). (d) Calculated charge density, $\rho_T(\mathbf{r})$, isosurfaces are shown on the side view. (e) Difference charge density $\Delta\rho_T(\mathbf{r})$ isosurfaces with electron depletion and accumulation zones described by green-yellow and turquoise, respectively, indicate that electrons donated to more electronegative C atoms leave the surface positively charged. (f) Band structure of CH ohs calculated using PBE featurede an indirect band gap of 3.82 eV, which is widened to 4.82 eV after HSE correction. Zero of energy is set to the maximum of the valence band. (g) Total (TDOS) and atom projected (PDOS) densities of states in arbitrary units. The energies of localized, magnetic (spin up, ↑ V and spin down, ↓ V) states due to the isolated H vacancy at A-site, and nonmagnetic states (DV) due to two H vacancies at adjacent A- and B-sites are indicated.

https://doi.org/10.1021/acs.jpcc.2c04453
J. Phys. Chem. C 2022, 126, 15491−15500

Table 1. Values Calculated for Bare C ohs, C_2H ohs and CH ohs Monolayers[a]

	E_b (eV)	ΔZ (e)	μ (μ_B)	State (eV)	Y_x (J/m^2)	Y_y (J/m^2)	ν_x (%)	ν_y (%)
C ohs	–	–	0	M	202.55	238.68	35	41
C_2H ohs	1.02	+0.1/+0.02	2.0	1.72/1.67	208.94	237.09	15	17
CH ohs	2.70	+0.1	0	3.82	191.33	210.63	18	20

[a]Average binding energy of hydrogen atom $\overline{E_b}$ (eV/atom); effective charge on H atoms ΔZ (e); magnetic moment μ (μ_B); electronic state, M metal, ferromagnetic semiconductor $E_{g,i,\uparrow}/E_{g,i,\downarrow}$ (eV), and semiconductor or insulator with indirect band gap $E_{g,i}$ (eV); Young's modulus, Y_x and Y_y (J/m^2); Poisson's ratio, ν_x and ν_y (%).

single sided hydrogen decoration induces dramatic changes in the mechanical, electronic and magnetic states of the 2D C ohs monolayer.

The full H coverage of C ohs monolayer, namely CH ohs, can be realized by completing half-coverage at one side to form first C_2H ohs and subsequently by repeating the same process for the remaining carbon atoms on the other side. This free-standing CH ohs monolayer is one of the energetically favorable hydrogenation geometries; it is dynamically and thermally stable and can be realized readily. It is reminiscent of the well-known graphane,[36−38] i.e., fully hydrogenated graphene, which is saturated by H alternatingly from both sides. All the relevant data about CH ohs obtained from first-principles calculations are presented in Figure 1c−f. The indirect band gap calculated by PBE is $E_{g,i}$ = 3.82 eV, which increases to 4.82 eV after HSE correction. Hence, the free-standing CH ohs monolayer is a stable, wide band gap semiconductor or an insulator. The calculated average binding energy of adsorbed H adatoms and relevant elastic properties are compared with bare C ohs and C_2H ohs monolayers in Table 1.

We now consider this CH ohs monolayer as a basic 2D structure and generate materials with novel physical and chemical properties via modulating dehydrogenation processes. First, a H-vacancy at the A-site, i.e. one H adatom is removed leaving one C atom at the A-site unsaturated, gives rise to two spin polarized (or spin degeneracy lifted) electronic states localized at that point. Accordingly, a filled, localized spin up state occurs ∼1.2 eV above the valence band edge; the empty, localized, spin down counterpart of it occurs ∼1.0 eV below the edge of the conduction band. Absorption peaks at ∼2.60 eV are thus expected in the optical spectrum. The energies of these localized states relative to the band edges differ slightly if the H-vacancy occurs at the B-site. If two H atoms are removed from adjacent sites (the first one, from the A-site at the upper side, the second one, from the B-site at the bottom side of the monolayer), one filled (empty) localized state occurs at the valence (conduction) band edge. Apparently, this process of removing one H atom from the CH ohs monolayer can be conceived as the reversal of the doping and hence is called here as antidoping, generating localized states in the band gap, which can be exploited for various electronic processes. Here we note a complex interplay between these localized states indicated in Figure 1g and the H vacancy migration, as well as the hole conduction.

Composite Structures. Through the modulating dehydrogenation of CH ohs, one can construct periodic composite structures consisting of adjacent hydrogen covered CH ohs and bare C ohs, commensurate stripes specified as or simply (n_y; m_y). Here, the subscript "*ohs*" is dropped, and n_y and m_y indicate, respectively, the widths of the CH ohs and C ohs stripes in terms of their number of primitive unit cells to make a supercell along *y*-axis taken as the direction of connected octagon rings. Accordingly, the stripes extend along *x*-direction with 1D translational periodicity of the primitive unit cell of each constituent. Before the analysis of diverse combinations and directions, (n_y; m_y) and (n_x; m_x), their dynamical and thermal stabilities have been assured. We found that the properties of these modulated structures depend on the widths and orientation of these stripes. These composite structures evolve to semiconductor-semiconductor or semiconductor-metal periodic heterostructures (junctions) with well-defined band-lineups or Schottky barrier, periodic 1D quantum structures ranging between two ultimate states, namely a wide band gap semiconductor (or insulator) and a good 2D metal. Earlier, patterned coverage of graphene by hydrogen were shown to lead to a band gap opening.[36−40] The present process uses the fully hydrogenated and bare C ohs on a monolayer; it is viable, versatile, and rather easy to realize without lattice matching problems at the interface between stipes.

Figure 2a shows composite structures, (n_y; m_y) with n_y = 1; m_y = 1, where carriers are confined periodically along the *y*-direction, but propagate along the *x*-axis. The electronic band structure and corresponding TDOS and LDOS calculated at the center of each stripe reveal that this composite structure behaves like a periodic heterostructure, despite the unique energy bands in momentum space. The band gap E_g = 1.73 eV between two bands derives from the orbitals in C ohs stripe. Within the Effective Mass Approximation (EMA), these bands can be viewed as if they derived from the states confined in the C ohs stripe, for which the edges of the gap E_g= ∼ 4.2 eV in the CH ohs stripe act as a potential barriers. Although the separation of wave functions in different stripes is not complete in this narrow composite structure, one can construct a band diagram with the valence, E_V, and conduction, E_C, band edges in the direct space as shown in the right panel. It depicts a normal band line-up with band offset energies indicated in the figure. This situation is better realized in the composite structure (n_y = 2; m_y = 2), in Figure 2b, where the periodic heterostructure consists of two different electronic materials. One side is a wide band gap semiconductor, and the other side has a narrow band gap of 0.6 eV. Accordingly, this heterostructure displays also a normal band line-up as shown in the band diagram in the direct space. The part with the narrow band gap can be considered representing two quantum wells (one for electrons, the other for holes) between the wide band gap parts; the band offset energies act as potential barriers. The energy level spacing varies approximately with ∼ n_y^{-2}. Hence, the states of four distinct bands with energy −2 eV < $E(k)$ < 2 eV, are confined in the C ohs stripe, which propagate along the *x*-direction. The upper two bands above E_F can be viewed as electronic states confined in the quantum well with 1.5 eV barrier; the lower two are hole states confined in the hole quantum well with 1.8 eV barrier as shown in Figure 2b. The dimensionality of the electronic states is

https://doi.org/10.1021/acs.jpcc.2c04453
J. Phys. Chem. C 2022, 126, 15491−15500

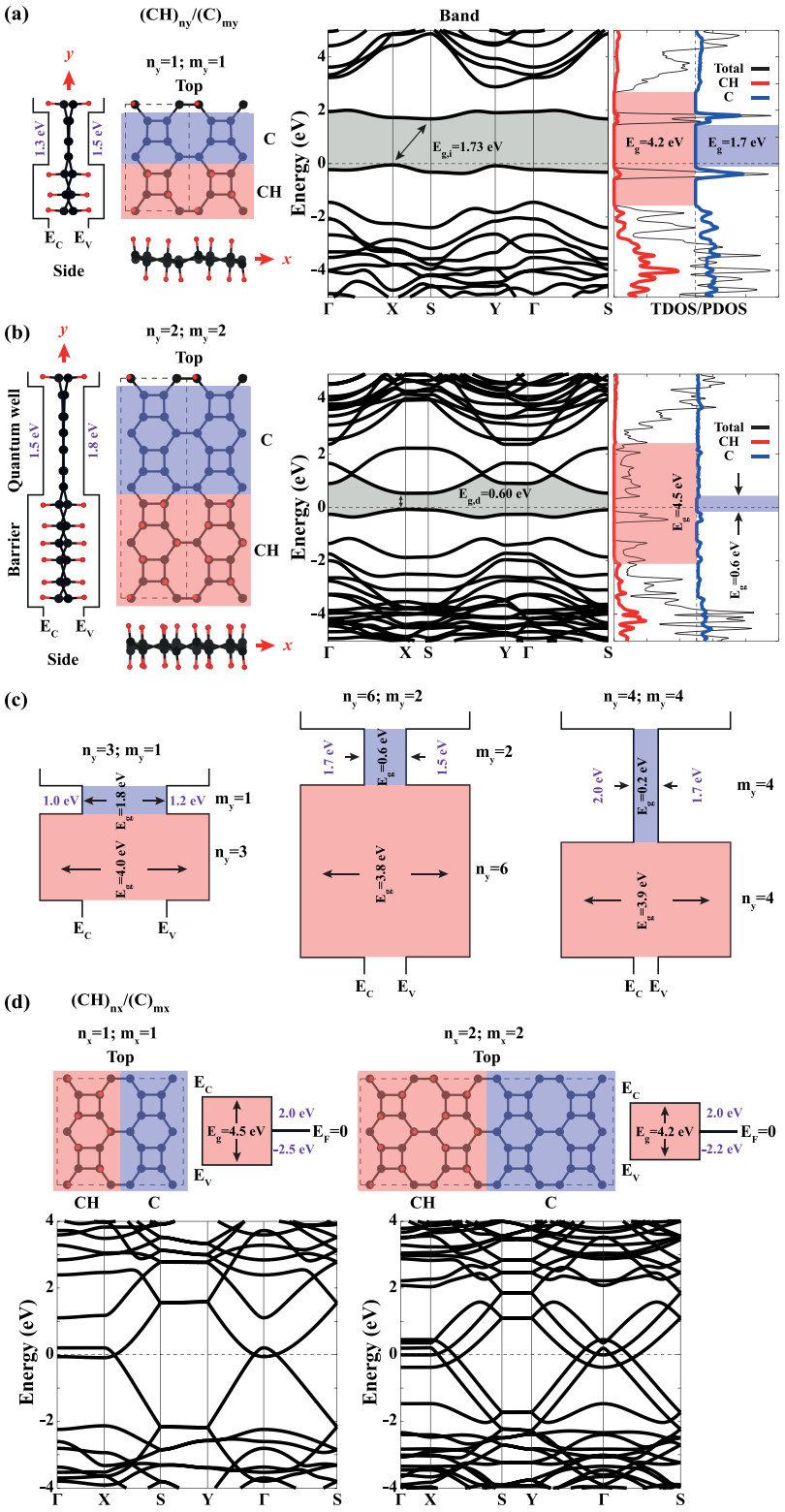

Figure 2. Various composite structure constructed from CH ohs. (a) Top and side views of the atomic arrangement of the composite structure $(CH)_{n_y}/(C)_{m_y}$ with $n_y = 1$; $m_y = 1$. Energy band diagram in the direct space is indicated with the edges of valence E_V and conduction E_C bands. Carbon and hydrogen atoms are shown by large-black and small-red balls, respectively. CH ohs (C ohs) stripes colored pink (blue-gray). Energy band structure in the momentum space, TDOS and the local density of states, LDOS calculated at the centers of CH ohs and C ohs stripes. (b) Same for the composite structure $n_y = 2$; $m_y = 2$. (c) Energy band diagram in direct space constructed from the electronic structure of for different composite structures calculated from the first-principles, such as $(n_y = 3; m_y = 1)$, $(n_y = 6; m_y = 2)$, $(n_y = 4; m_y = 4)$. Normal band line-up energies are indicated. (d) Atomic configuration, energy band diagram and energy band structure of the composite structures $(CH)_{n_x}/(C)_{m_x}$ calculated for $(n_x = 1; m_x = 1)$ and $(n_x = 2; m_x = 2)$.

https://doi.org/10.1021/acs.jpcc.2c04453
J. Phys. Chem. C 2022, 126, 15491−15500

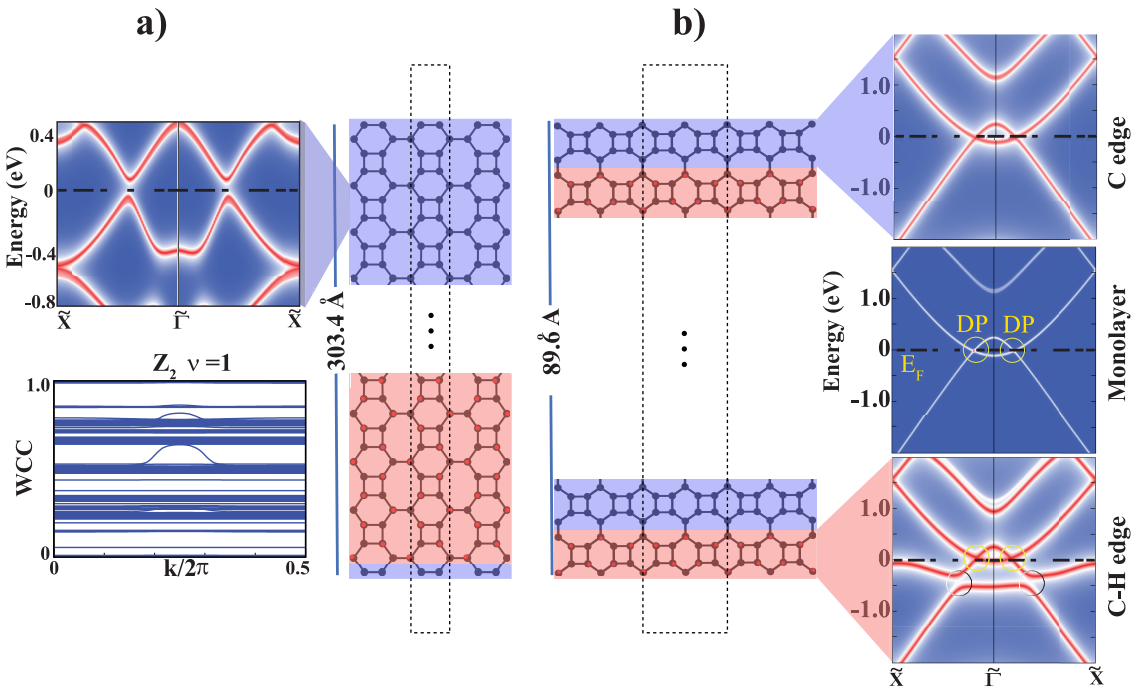

Figure 3. Topological edge states of composite nanoribbons composed of CH ohs and C ohs 2D stripes along *x*- and *y*-directions. (a) Top view of the atomic structure of composite nanoribbon ($n_y = 4$; $m_y = 4$), with stripes along *x*-direction, but the confinement along *y*-direction. The unit cells are delineated. The nanoribbon has CH ohs and C ohs termination at the upper and lower edges, respectively. The calculated edge states and time evolution of wannier charge centers (WCC) at the $k_z = 0$ surface for nontrivial free-standing of monolayer. (b) Top view of the atomic structure of composite nanoribbon ($n_x = 1$; $m_x = 1$), with stripes along *y*-direction, but the confinement along *x*-direction. The edges are terminated by C ohs and CH ohs. Upper panel, upper edge states; middle panel, projected bulk states; lower panel, bottom edge states. The edge states are depicted by red lines; DP stands for Dirac like points. The zero of energy is set at the Fermi level.

reflected in the dispersion of bands in the momentum space; these four bands are dispersive along the $\Gamma - X$ direction, but flat along the $\Gamma - Y$ direction. Moreover, the density of states of 1D bands propagating along *x*-direction, but confined along *y*- and *z*-directions retains the well-known $\sim 1/\sqrt{E}$ signature. On the other hand, states with energies beyond the band gap of the CH ohs stripe propagate also along the *y*-direction.

The interplay between the widths of CH and C ohs stripes specified by n_y and m_y, and the associated electronic structures are summarized through the bands diagrams of ($n_y = 3$;$m_y = 1$), ($n_y = 6$;$m_y = 2$), ($n_y = 4$;$m_y = 4$) presented in Figure 2c. In the left panel, the band diagram and the periodic quantum well structures derived thereof are similar to that of ($n_y = 1$;$m_y = 1$). In the middle panel, the band diagram revealed from ($n_y = 6$;$m_y = 2$) continues to reflect a periodic semiconductor-semiconductor heterostructure, but both band gaps in the barrier and well regions are reduced due to their increasing widths (hence decreasing confinement). In ($n_y = 4$;$m_y = 4$) structure, the band gap in C ohs reduces to 0.2 eV with increasing m_y, but that in CH ohs increases with decreasing n_y relative to the previous case. Our analysis of LDOS calculated at each atom of two adjacent stripes reveals that the band diagram in the direct space is rather uniform and the interface region of charge depletion/accumulation is not wide. The transition from one band gap to the other is completed within |**b**|/2. Our further analysis of the ($n_y = 6$;$m_y = 6$) composite structure is also consistent with the above findings; it exhibits always a band gap in C ohs stripes, even if very small. However, if the confinement direction is changed from *y*- to *x*-direction, the situation becomes different; the C ohs stripe extending along the *y*-direction becomes metallic even for ($n_x = 1$;$m_x = 1$) as seen Figure 2d. The energy band structure and band diagrams in direct space calculated for ($n_x = 1$; $m_x = 1$) and ($n_x = 2$;$m_x = 2$) depict periodic semiconductor−metal heterostructures, wherein the height of the Schottky barrier is a critical feature for various diode functions.[41,42]

Here we note an interesting feature revealed in the electronic energy bands of composite structures (n_y; m_y) and (n_x; m_x). The bands of the former do not cross no matter what the value of m_y is. In contrast, the bands of the latter cross in the C ohs stripe even for a small value of $m_x = 1$. Notably, a similar situation occurs also in the armchair and zigzag graphene nanoribbons. Here, we explored the features of this puzzling situation in the topological properties of nanoribbons of the above composite structures having confinement in *y*- and *x*-directions, respectively. In fact, after graphene has been predicted to possess the quantum Hall states, and also other group IV elements in the honeycomb network, like silicene and germanene, were shown to have nontrivial topological properties due to spin orbit coupling (SOC).[43] Moreover, recent studies have revealed that all sp^2-bonded carbon networks can form topological nodal rings, while sp^2−sp^3 hybrid network structures can have topological nodal lines. Besides, some graphene networks constitute a new class of materials, which have Dirac surface semimetals with 3D Weyl-surface.[44] Even if a thorough study of the topological properties of all the above composite structures and CH ohs are beyond the scope of this study, the analysis of two nanoribbons described in Figure 3 can be sufficient to conceive their topological characters and to understand the puzzling relation between band crossing in momentum space and directionality of wave function propagation in direct space.

https://doi.org/10.1021/acs.jpcc.2c04453
J. Phys. Chem. C 2022, 126, 15491−15500

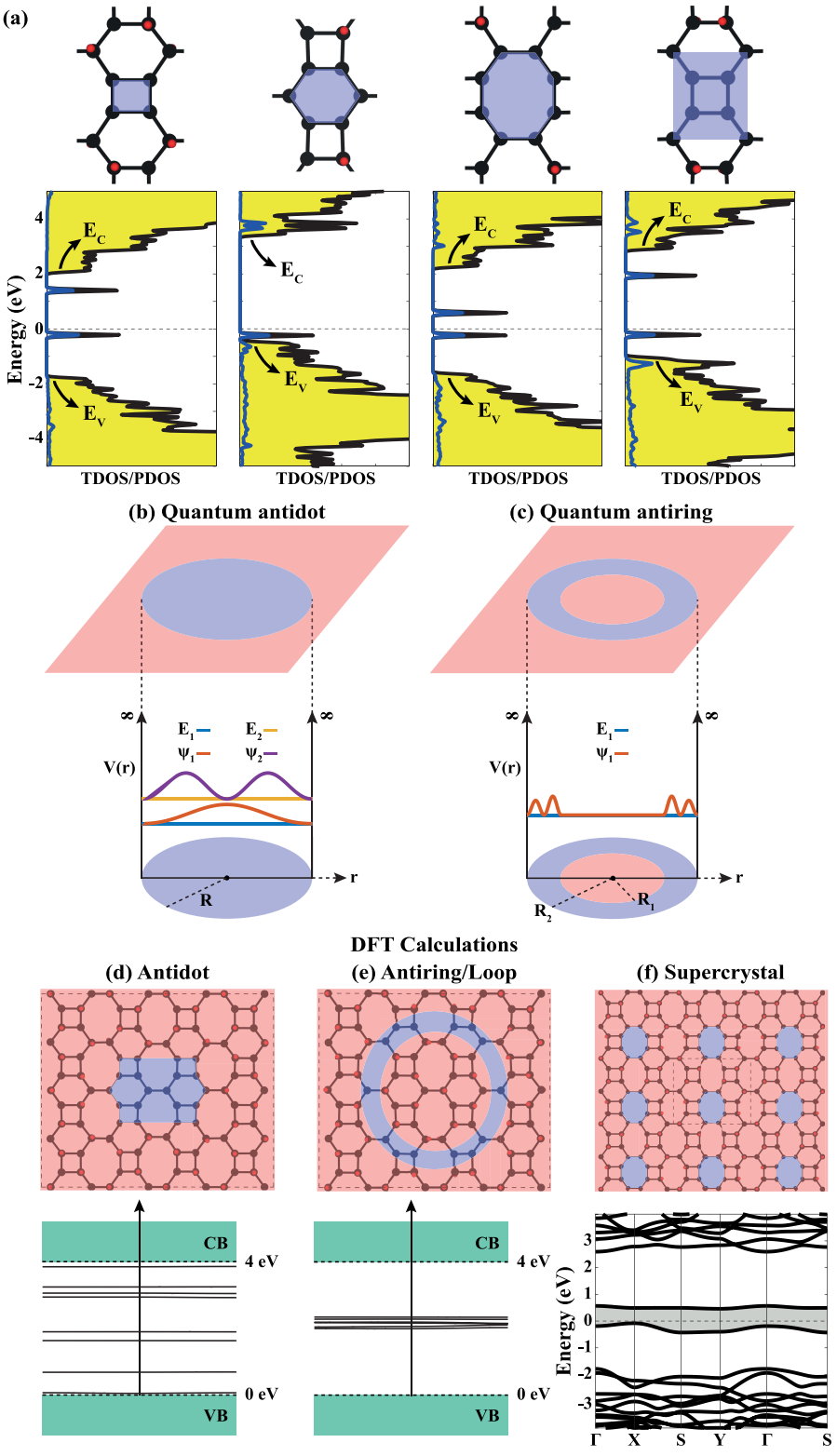

Figure 4. (a) Localized gap states constructed by removing H atoms from host C atoms forming a single square, hexagon, octagon rings, and double rectangle. Localized states close to E_V are occupied; those close to E_C are unoccupied. The resonance states in the band continua are not shown. The zero of energy is set to the Fermi level. (b) Model structure of a quantum antidot constructed by removing all saturating H adatoms within a circle of radius R. Corresponding cylindrical quantum well model with infinite barrier. Only first and second energy eigenvalue states and corresponding wave functions are shown. (c) Model structure of a quantum antiring constructed by removing H adatoms in a ring within $R_1 < r < R_2$. Corresponding cylindrical quantum shell model with the lowest energy eigenvalue. (d) Quantum antidot structure constructed by removing 20 saturating H adatoms in a rectangular zone of CH ohs and corresponding energy level diagram calculated by fully optimized structure within PBE. (e) Same for quantum antiring. (f) Supercrystal model realized on CH ohs. Zones of monolayer covered (uncovered) by H atoms are colored pink (blue-gray).

https://doi.org/10.1021/acs.jpcc.2c04453
J. Phys. Chem. C 2022, 126, 15491−15500

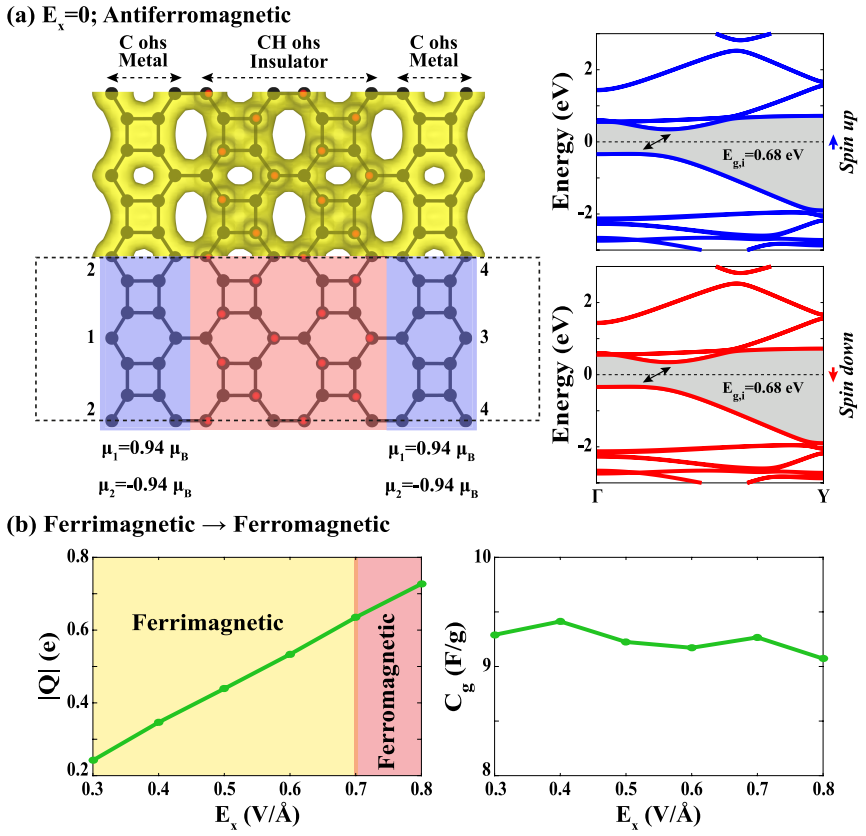

Figure 5. Nanoscale capacitor model, $(C)_{m_x=1}/(CH)_{n_x=2}/(C)_{m_x=1}$. (a) Atomic structure in the unit cell is shaded and the total charge density $\rho(\mathbf{r})$ is presented in the adjacent unit cell. The magnetic moments of C atoms at the zigzag edges identified by numerals indicate an antiferromagnetic ground state for $E_x < 0.3$ V/Å. Spin polarized bands for spin up and spin down states at $E_x = 0$. (b) Variation of the magnitude of the average charge $|Q|$ accumulated at C ohs stripes and calculated gravimetric capacitance C_g as a function electric field applied across the nanoscale capacitor, E_x.

Notably, the edge states of 1D nanoribbons are critical like the surface states of 2D monolayers.

In order to determine the topological behavior of the ($n_y = 4$ and $m_y = 4$) composite monolayer, we consider the Z_2 invariant ν expressed as $(-1)^{\nu} = \prod_{i=1}^{n} \delta_i$ ($n = 4$ in 2D)[45,46] and calculate it equal to 1. Furthermore, the Z_2 topological invariant ν can be evaluated by the Wannier charge center (WCC) evolution or Wilson loop method.[45] The WCC is related to the edge states that are protected by time reversal symmetry (TRS). For a TRS insulator, WCC consists of Kramer pairs due to the TRS (see Figure 3a) and the topological indicator, $\nu = 1$. This indicates that the ($n_y = 4$ and $m_y = 4$) monolayer has a nontrivial topological order. To further confirm the topological properties of ($n_y = 4$ and $m_y = 4$) scaffold, we examined the edge states in Figure 3a. Since one nodal line is inner and the other is outer, they will cancel each other resulting in a band gap. Accordingly, the system becomes a topological insulator (TI). As for the composite structure ($n_x = 1$; $m_x = 1$), the bands of it cross along Y−Γ−S directions of the Brillouin zone, which can be classified as a nodal line semimetal. The topological Z_2 invariant ν calculated to be zero confirms that the ($n_x = 1$; $m_x = 1$) structure cannot be a Z_2 TI. One of the most important fingerprint of topological nodal line semimetals is the existence of topologically protected edge states outside or inside of the nodal point. The atomic structure of zigzag-edged nanoribbons of this monolayer with different termination and the pertaining analysis are presented in Figure 3b. The edge states of this composite nanoribbon can be separated from those of ($n_x = 1$; $m_x = 1$). Since the nodal line is projected onto the zigzag edge nanoribbon, it yields a topologically protected edge states outside the nodal point. When spin−orbit coupling is neglected, this composite nanoribbon contains a topologically protected edge states outside the Dirac nodal point. It means that $n_x = 1$; $m_x = 1$ monolayer is a topological nodal line semimetal.

Antidot, Antiring, and Supercrystals. Next, we consider H atoms are removed from C atoms at the corners of square, hexagon, octagon, and double rectangle in Figure 4a and show their localized states in the band gap of the CH ohs monolayer. The peaks close to the edge of the valence band correspond to occupied localized states; and those close to the edge of the conduction band are unoccupied. Since even number of adjacent H adatoms are removed, the localized gap states are nonmagnetic. The energy location of these localized gap states provides a tunability. In addition, the resonance states in the band continua are also created upon the removal of H adatoms.

In parts b and c of Figure 4, we first treat simple quantum models based on EMA for antidot and antiring formed in a CH ohs monolayer for the sake of better understanding of the underlying physics. The antidot is constituted by the dehydrogenation of CH ohs in a round, disc like zone, $r < R$, whereas the dehydrogenation takes place in a ring-like zone, $R_1 < r < R_2$ for the antiring. Hence, the electrons are confined to the areas, where H atoms removed, so that $V(r) = 0$ for $r < R$; but for $r > R$ the wide band gap of CH ohs zone acts as if a potential barrier, $V(r) > 0$. Here, for the simplicity in analytical

https://doi.org/10.1021/acs.jpcc.2c04453
J. Phys. Chem. C 2022, 126, 15491−15500

calculations, we take $V(r) \rightarrow \infty$ for $r > R$. In the case of the antiring, $V(r) = 0$ for $R_1 < r < R_2$ inside the ringlike zone, but $V(r) \rightarrow \infty$ for $r < R_1$ and $r > R_2$. It should be noted that these 0D structures differ from the artificial atoms:[47] core (quantum dot), shell (quantum ring)[48,49] and core−shell structures,[50,51] nanoflakes,[52] and quantum antidots.[53]

The solutions of these cylindrical and cylindrical shell potentials with an infinite barrier can be expressed in terms of Bessel and Neumann functions.[54,55] The wave functions of the antidot are expressed in terms of Bessel functions $J_l(kr)$ of order l:

$$\Psi_{n,l}(r, \phi) = \frac{1}{\sqrt{2\pi}} J_l(kr) \exp(\pm il\phi),\ l = 0,1,2. \quad (1)$$

with the boundary condition: $J_l(kR) = 0$ leading to k_z/R where z are zeroes of cylindrical Bessel function and energy eigenvalues $E_l = \hbar^2k^2/2m^*$, where m^* is the effective mass of electrons. In the case of the antiring with cylindrical shell potential,

$$\Psi_{n,l}(r, \phi) = \frac{1}{\sqrt{2\pi}} [c_1 J_l(kr) + c_2 N_l(kr)] \exp(\pm il\phi),$$
$$l = 0, 1, 2. \quad (2)$$

where $N_l(kr)$ is the Neumann function of order l with the boundary condition, $\Psi_{n,l}(R_1, \phi) = \Psi_l(R_2, \phi) = 0$.

The energy level diagram and the corresponding wave functions obtained from this model based on EMA are depicted in Figure 4, parts b and c.

In view of these models based on EMA, we now study realistic antidot, antiring, and supercrystal constructed on the CH ohs monolayer through its dehydrogenation according to a preset pattern. In Figure 4d, the antidot is formed by removing 20 H atoms from C atoms positioned in a shaded, rectangular region. The occupied and empty dot states shown in the band gap justify the above model derived from EMA. The level spacing of these states depend on the size and geometry of confining zone and hence can be monitored. The ring like loop of C ohs formed on the CH monolayer in Figure 4e confines also several tightly spaced occupied and empty states. The supercrystal model in Figure 4f is constructed by removing H atoms at the corners of octagons, which act as attractive potential for electrons and give rise to the band structure depicted in the figure. The system becomes an indirect band gap semiconductor with $E_{g,i} = 0.54$ eV. The band structure can be monitored by the size, geometry and repeat periods of dehydrogenated zones. Similar supercrystals can be formed by the hydrogenation of periodic zones on C ohs of diverse size and symmetry.

Magnetic Nanoscale Capacitors. Now we point out an important application achievable with the composite structures, which display diverse magnetic states depending on the electric field. An insulating CH ohs stripe between two metallic C ohs ones can be combined into single or series connected Helmholtz capacitors[56,57] as depicted in Figure 5a. In fact, such an in-plane nanoscale capacitor can be constructed by forming an CH ohs stripe through hydrogenation of a stripe at the center of a zigzag edged C ohs nanoribbon and hence by leaving two bare C ohs stripes at both sides. The widths of CH ohs stripes, n_x and that of C ohs, m_x can be set to a desired value as parameters of this device. The charging of the capacitor is achieved by an external electric field applied across the capacitor, E_x, in the open circuit; it is a reverse situation in the operation of the capacitor in closed circuit. Initially, for $E_x = 0$, each 2-fold coordinated C atoms at both zigzag edges of the in-plane nanocapacitor has a magnetic moment of $\mu \pm 0.94\ \mu_B$. These magnetic moments display an antiferromagnetic order. Accordingly, the system is an antiferromagnetic semiconductor with an indirect band gap for both spin up and spin down bands as shown in Figure 5a. When $E_x \geq 0.3$ V/Å, the band gaps are closed and excess charge $\pm Q$ starts to accumulate on the metallic C ohs stripes. At that instant, the antiferromagnetic state changes to a ferrimagnetic state. For $E_x = 0.5$ V/Å, the total magnetic moment is calculated to be $\mu_T = 0.45\ \mu_B$/cell. Interestingly, this ferrimagnetic state remains for increasing E_x or increasing charge $|Q|$ for awhile, but it switches to the ferromagnetic state for $E_x \geq 0.7$ V/Å.

The gravimetric capacitance is calculated from the expression $C_g = Q^2/2M_cE_s$, where the total energy difference is $E_s = E_T(E_x) - E_T(E_x = 0)$, and M_c is the mass of the system. In Figure 5b, the variations of the average charge $|Q|$ in the metallic C ohs stripes and the calculated gravimetric capacitance as a function of the applied electric field are shown. The gravimetric capacitance value, C_g attained in the present system is quite high owing to the nanoscale size of the device and hence is comparable with that of supercapacitors. The values of gravimetric capacitance and also capacitance C can be changed by varying n_x and m_x, even if the response is not linear due to interface effects. Generally, the capacitance increases as n_x increases but decreases as n_x increases. On the other hand, the decrease of n_x is limited by Zener breakdown. As example, we calculated $C_g = 14.9$ F/g for $n_x = 1$, $m_x = 1$, but $C_g = 6.7$ F/g for $m_x = 1$, $n_x = 3$. Upon increasing the widths of metallic plates $m_x = 2$, while keeping $n_x = 2$, C_g decreased to 6.5 F/g due to interface effects.

We believe that the planar, nanoscale capacitor proposed here may offer potential applications in flexible nanoelectronics, such as charge and energy storage devices and diverse sensors. Further to the nanoscale capacitor, one can also envisage a resonant tunneling double barrier constructed from C/CH/C/CH/C ohs stripes. Finally, one can consider also capacitor models constructed from the vertical stacking of insulating CH ohs monolayers capped by the metallic C ohs ones.

CONCLUSIONS

While each carbon atom of C ohs forms sp^2-like hybrid bonds with three nearest neighbors, p_z-like orbitals cross the Fermi level attributing a good 2D metallicity to the monolayer. Once each p_z-like orbital is saturated with a H adatom, C ohs turns to CH ohs, whereby their C−H bonds form bonding and antibondig states. Upon interacting with neighbors, they evolve and disperse to the edges of valence and conduction bands, which, in turn, open a wide band gap in the metallic density of states. Removing a single H atom gives rise to localized, magnetic states in the band gap, similar to impurity states. When the saturation of dangling p_z-orbitals by H adatoms in a specific region of metallic C ohs is achieved according to a present form, this region of C ohs attains a wide band gap, which represents a potential barrier for the states derived from unsaturated p_z-like orbitals of C ohs. Eventually, these states become confined in the wells surrounded by potential barriers and make metals or narrow band gap semiconductors joined to wide band gap CH ohs regions. In view of these arguments derived from EMA, we demonstrated from first-principles calculations that one can construct periodic or finite size

https://doi.org/10.1021/acs.jpcc.2c04453
J. Phys. Chem. C 2022, 126, 15491−15500

composite structures showing diverse device characteristics. These are semiconductor-semiconductor or semiconductor-metal heterostructures, quantum antidots and antirings, single or series connected nanocapacitors, and resonant tunneling structures. All these devices can be fabricated commensurately without any lattice mismatch restriction. Notably, the above devices can readily be constituted on appropriate substrates, since neither C ohs, nor CH ohs monolayers formed on substrates would be affected electronically.[8,9]

Additionally, we demonstrated that not only hydrogenated C ohs, but also hydrogenated Si ohs, as well as C ohs or Si ohs covered by other elements, such as oxygen, alkali halide, and rare-earth atoms can be realized. In particular, one can construct magnetic 2D monolayers with magnetic ground states above room temperature, which vary with coverage symmetry and layer number. We believe that the process proposed in this study may develop *a new paradigm* in nanocircuitry.

AUTHOR INFORMATION

Corresponding Authors

Ethem Aktürk − *Department of Physics, Adnan Menderes University, 09100 Aydin, Turkey; Physik Department E20, Technische Universität München, 85748 Garching, Germany;* orcid.org/0000-0002-1615-7841; Email: ethem.aktuerk@tum.de

Salim Ciraci − *Department of Physics, Bilkent University, Ankara 06800, Turkey*; Email: ciraci@fen.bilkent.edu.tr

Authors

Salih Demirci − *Department of Physics, Kırıkkale University, Kırıkkale 71450, Turkey;* orcid.org/0000-0002-1272-9603

Taylan Gorkan − *Department of Physics, Adnan Menderes University, 09100 Aydin, Turkey; Materials Science and Engineering, School for Engineering of Matter, Transport and Energy, Arizona State University, Tempe, Arizona 85287, United States*

Şafak Çallıoğlu − *Department of Electrical and Electronic Engineering, Bilkent University, Ankara 06800, Turkey; Department of Physics, Bilkent University, Ankara 06800, Turkey*

V. Ongun Özçelik − *Department of Natural and Mathematical Sciences, Ozyegin University, Istanbul 34794, Turkey; Department of Electrical and Computer Engineering, University of Minnesota, Minneapolis, Minnesota 55455, United States;* orcid.org/0000-0003-0645-7231

Johannes V. Barth − *Physik Department E20, Technische Universität München, 85748 Garching, Germany*

Complete contact information is available at: https://pubs.acs.org/10.1021/acs.jpcc.2c04453

Notes

The authors declare no competing financial interest.

ACKNOWLEDGMENTS

S.C. thanks TÜBA, The Academy of Science of Turkey for the financial support. E.A. acknowledges the Alexander von Humboldt Foundation for a Research Fellowship for Experienced Researchers. T.G. was supported by the Scientific and Technological Research Council of Turkey (TUBITAK) under the 2214 scholarship. V.O.O. was supported by the BAGEP Award of the Science Academy. Computations were performed at the National Center for High-Performance Computing of Turkey (UHeM) under Grant No. 5004132016 and under Project Numbers 2022/003 and 2022/004 by the Scientific Research Projects Coordination Unit of Kırıkkale University, TUBITAK ULAKBIM, High Performance and Grid Computing Center (TR-Grid e-Infrastructure), and the Leibniz Supercomputing Centre.

REFERENCES

(1) Balaban, A.; Rentia, C. C.; Ciupitu, E. Chemical graphs. 6. Estimation of relative stability of several planar and tridimensional lattices for elementary carbon. *Revue Roumaine de Chimie* **1968**, *13*, 231.

(2) Hudspeth, M. A.; Whitman, B. W.; Barone, V.; Peralta, J. E. Electronic properties of the biphenylene sheet and its one-dimensional derivatives. *ACS Nano* **2010**, *4*, 4565−4570.

(3) Wang, X.-Q.; Li, H.-D.; Wang, J.-T. Prediction of a new two-dimensional metallic carbon allotrope. *Phys. Chem. Chem. Phys.* **2013**, *15*, 2024−2030.

(4) Rahaman, O.; Mortazavi, B.; Dianat, A.; Cuniberti, G.; Rabczuk, T. Metamorphosis in carbon network: From penta-graphene to biphenylene under uniaxial tension. *FlatChem.* **2017**, *1*, 65−73.

(5) Shahrokhi, M.; Mortazavi, B.; Berdiyorov, G. R. New two-dimensional boron nitride allotropes with attractive electronic and optical properties. *Solid State Commun.* **2017**, *253*, 51−56.

(6) He, C.; Wang, W. 2D Octagon-Structure Carbon and Its Polarization Resolved Raman Spectra. *Nanomaterials* **2020**, *10*, 2252.

(7) Schlütter, F.; Nishiuchi, T.; Enkelmann, V.; Müllen, K. Octafunctionalized Biphenylenes: Molecular Precursors for Isomeric Graphene Nanostructures. *Angew. Chem., Int. Ed.* **2014**, *53*, 1538−1542.

(8) Fan, Q.; Yan, L.; Tripp, M. W.; Krejčí, O.; Dimosthenous, S.; Kachel, S. R.; Chen, M.; Foster, A. S.; Koert, U.; Liljeroth, P.; et al. Biphenylene network: A nonbenzenoid carbon allotrope. *Science* **2021**, *372*, 852−856.

(9) Demirci, S.; Çallıoğlu, Ş.; Gorkan, T.; Aktürk, E.; Ciraci, S. Stability and electronic properties of monolayer and multilayer structures of group-IV elements and compounds of complementary groups in biphenylene network. *Phys. Rev. B* **2022**, *105*, 035408.

(10) Şahin, H.; Cahangirov, S.; Topsakal, M.; Bekaroglu, E.; Akturk, E.; Senger, R. T.; Ciraci, S. Monolayer honeycomb structures of group-IV elements and III-V binary compounds: First-principles calculations. *Phys. Rev. B* **2009**, *80*, 155453.

(11) Cahangirov, S.; Topsakal, M.; Aktürk, E.; Şahin, H.; Ciraci, S. Two-and one-dimensional honeycomb structures of silicon and germanium. *Physical review letters* **2009**, *102*, 236804.

(12) Topsakal, M.; Aktürk, E.; Ciraci, S. First-principles study of two-and one-dimensional honeycomb structures of boron nitride. *Phys. Rev. B* **2009**, *79*, 115442.

(13) Bekaroglu, E.; Topsakal, M.; Cahangirov, S.; Ciraci, S. First-principles study of defects and adatoms in silicon carbide honeycomb structures. *Phys. Rev. B* **2010**, *81*, 075433.

(14) Topsakal, M.; Cahangirov, S.; Bekaroglu, E.; Ciraci, S. First-principles study of zinc oxide honeycomb structures. *Phys. Rev. B* **2009**, *80*, 235119.

(15) Novoselov, K. S.; Geim, A. K.; Morozov, S. V.; Jiang, D.-e.; Zhang, Y.; Dubonos, S. V.; Grigorieva, I. V.; Firsov, A. A. Electric field effect in atomically thin carbon films. *science* **2004**, *306*, 666−669.

(16) Liao, Y.; Shi, X.; Ouyang, T.; Li, J.; Zhang, C.; Tang, C.; He, C.; Zhong, J. New Two-Dimensional Wide Band Gap Hydrocarbon Insulator by Hydrogenation of a Biphenylene Sheet. *J. Phys. Chem. Lett.* **2021**, *12*, 8889−8896.

(17) Liu, T.; Jing, Y.; Li, Y. Two-Dimensional Biphenylene: A Graphene Allotrope with Superior Activity toward Electrochemical Oxygen Reduction Reaction. *J. Phys. Chem. Lett.* **2021**, *12*, 12230−12234.

(18) Lee, S.; Singh, A.; Lee, H. Band gap engineering of 2D biphenylene carbon sheets with hydrogenation. *Journal of the Korean Physical Society* **2021**, *79*, 846−850.
(19) Zhang, P.; Ouyang, T.; Tang, C.; He, C.; Li, J.; Zhang, C.; Hu, M.; Zhong, J. The intrinsic thermal transport properties of the biphenylene network and the influence of hydrogenation: a first-principles study. *Journal of Materials Chemistry C* **2021**, *9*, 16945−16951.
(20) Gorkan, T.; Çallıoğlu, Ş.; Demirci, S.; Aktürk, E.; Ciraci, S. Functional Carbon and Silicon Monolayers in Biphenylene Network. *ACS Appl. Electron. Mater.* **2022**, *4*, 3056−3070.
(21) Obeid, M. M.; Sun, Q. Assembling biphenylene into 3D porous metallic carbon allotrope for promising anode of lithium-ion batteries. *Carbon* **2022**, *188*, 95−103.
(22) Sun, W.; Shen, Y.; Ni, D.; Wang, Q. A biphenylene nanoribbon-based 3D metallic and ductile carbon allotrope. *Nanoscale* **2022**, *14*, 3801−3807.
(23) Kresse, G.; Furthmüller, J. Efficient iterative schemes for ab initio total-energy calculations using a plane-wave basis set. *Phys. Rev. B* **1996**, *54*, 11169.
(24) Blöchl, P. E. Projector augmented-wave method. *Phys. Rev. B* **1994**, *50*, 17953.
(25) Perdew, J. P.; Burke, K.; Ernzerhof, M. Generalized gradient approximation made simple. *Physical review letters* **1996**, *77*, 3865.
(26) Grimme, S.; Antony, J.; Ehrlich, S.; Krieg, H. A consistent and accurate ab initio parametrization of density functional dispersion correction (DFT-D) for the 94 elements H-Pu. *J. Chem. Phys.* **2010**, *132*, 154104.
(27) Grimme, S.; Ehrlich, S.; Goerigk, L. Effect of the damping function in dispersion corrected density functional theory. *Journal of computational chemistry* **2011**, *32*, 1456−1465.
(28) Monkhorst, H. J.; Pack, J. D. Special points for Brillouin-zone integrations. *Phys. Rev. B* **1976**, *13*, 5188.
(29) Krukau, A. V.; Vydrov, O. A.; Izmaylov, A. F.; Scuseria, G. E. Influence of the exchange screening parameter on the performance of screened hybrid functionals. *J. Chem. Phys.* **2006**, *125*, 224106.
(30) Wu, Q.; Zhang, S.; Song, H.-F.; Troyer, M.; Soluyanov, A. A. WannierTools: An open-source software package for novel topological materials. *Comput. Phys. Commun.* **2018**, *224*, 405−416.
(31) Mostofi, A. A.; Yates, J. R.; Pizzi, G.; Lee, Y.-S.; Souza, I.; Vanderbilt, D.; Marzari, N. An updated version of wannier90: A tool for obtaining maximally-localised Wannier functions. *Comput. Phys. Commun.* **2014**, *185*, 2309−2310.
(32) Soler, J. M.; Artacho, E.; Gale, J. D.; García, A.; Junquera, J.; Ordejón, P.; Sánchez-Portal, D. The SIESTA method for ab initio order-N materials simulation. *J. Phys.: Condens. Matter* **2002**, *14*, 2745.
(33) Togo, A.; Tanaka, I. First principles phonon calculations in materials science. *Scripta Materialia* **2015**, *108*, 1−5.
(34) Henkelman, G.; Arnaldsson, A.; Jónsson, H. A fast and robust algorithm for Bader decomposition of charge density. *Comput. Mater. Sci.* **2006**, *36*, 354−360.
(35) Momma, K.; Izumi, F. VESTA 3 for three-dimensional visualization of crystal, volumetric and morphology data. *Journal of applied crystallography* **2011**, *44*, 1272−1276.
(36) Sofo, J. O.; Chaudhari, A. S.; Barber, G. D. Graphane: A two-dimensional hydrocarbon. *Phys. Rev. B* **2007**, *75*, 153401.
(37) Elias, D. C.; Nair, R. R.; Mohiuddin, T. M. G.; Morozov, S. V.; Blake, P.; Halsall, M. P.; Ferrari, A. C.; Boukhvalov, D. W.; Katsnelson, M. I.; Geim, A. K.; et al. Control of Graphene's Properties by Reversible Hydrogenation: Evidence for Graphane. *Science* **2009**, *323*, 610−613.
(38) Şahin, H.; Ataca, C.; Ciraci, S. Electronic and magnetic properties of graphane nanoribbons. *Phys. Rev. B* **2010**, *81*, 205417.
(39) Balog, R.; Jørgensen, B.; Nilsson, L.; Andersen, M.; Rienks, E.; Bianchi, M.; Fanetti, M.; Lægsgaard, E.; Baraldi, A.; Lizzit, S.; et al. Bandgap opening in graphene induced by patterned hydrogen adsorption. *Nature materials* **2010**, *9*, 315−319.
(40) Şahin, H.; Ciraci, S. Structural, mechanical, and electronic properties of defect-patterned graphene nanomeshes from first principles. *Phys. Rev. B* **2011**, *84*, 035452.
(41) Aras, M.; Kılıç, i. m. c.; Ciraci, S. Planar heterostructures of single-layer transition metal dichalcogenides: Composite structures, Schottky junctions, tunneling barriers, and half metals. *Phys. Rev. B* **2017**, *95*, 075434.
(42) Aras, M.; Kılıç, Ç.; Ciraci, S. Lateral and Vertical Heterostructures of Transition Metal Dichalcogenides. *J. Phys. Chem. C* **2018**, *122*, 1547−1555.
(43) Liu, C.-C.; Feng, W.; Yao, Y. Quantum Spin Hall Effect in Silicene and Two-Dimensional Germanium. *Phys. Rev. Lett.* **2011**, *107*, 076802.
(44) Wang, J.-T.; Weng, H.; Chen, C. Topological nodal line semimetals in graphene network structures. *Advances in Physics: X* **2019**, *4*, 1625724.
(45) Kane, C. L.; Mele, E. J. Quantum Spin Hall Effect in Graphene. *Phys. Rev. Lett.* **2005**, *95*, 226801.
(46) Bansil, A.; Lin, H.; Das, T. Colloquium: Topological band theory. *Rev. Mod. Phys.* **2016**, *88*, 021004.
(47) Ashoori, R. Electrons in artificial atoms. *Nature* **1996**, *379*, 413−419.
(48) Chen, Q.; Li, L. L.; Peeters, F. M. Inner and outer ring states of MoS 2 quantum rings: Energy spectrum, charge and spin currents. *J. Appl. Phys.* **2019**, *125*, 244303.
(49) Topalović, D. c. v. B.; Arsoski, V. V.; Tadić, M. i. c. v.; Peeters, F. m. c. M. Confined electron states in two-dimensional HgTe in magnetic field: Quantum dot versus quantum ring behavior. *Phys. Rev. B* **2019**, *100*, 125304.
(50) Cahangirov, S.; Ciraci, S. Two-dimensional C/BN core/shell structures. *Phys. Rev. B* **2011**, *83*, 165448.
(51) Sandner, A.; Preis, T.; Schell, C.; Giudici, P.; Watanabe, K.; Taniguchi, T.; Weiss, D.; Eroms, J. Ballistic transport in graphene antidot lattices. *Nano Lett.* **2015**, *15*, 8402−8406.
(52) Aktürk, O. Ü.; Aktürk, E.; Gürel, H.; Ciraci, S. Tunable dynamics of a flake on graphene: libration frequency. *Phys. Rev. B* **2017**, *95*, 125413.
(53) Vanević, M.; Stojanović, V. M.; Kindermann, M. Character of electronic states in graphene antidot lattices: Flat bands and spatial localization. *Phys. Rev. B* **2009**, *80*, 045410.
(54) Even, J.; Loualiche, S. Exact analytical solutions describing quantum dot, ring and wire wavefunctions. *Journal of Physics A: Mathematical and General* **2004**, *37*, L289.
(55) Harry, S.; Adekanmbi, M. Confinement Energy of Quantum Dots and the Brus Equation. *International Journal of Research-Granthaalayah* **2020**, *8*, 318−323.
(56) Özçelik, V. O.; Ciraci, S. Nanoscale dielectric capacitors composed of graphene and boron nitride layers: a first-principles study of high capacitance at nanoscale. *J. Phys. Chem. C* **2013**, *117*, 15327−15334.
(57) Özçelik, V. O.; Ciraci, S. High-performance planar nanoscale dielectric capacitors. *Phys. Rev. B* **2015**, *91*, 195445.

https://doi.org/10.1021/acs.jpcc.2c04453
J. Phys. Chem. C 2022, 126, 15491−15500